ACS APPLIED MATERIALS & INTERFACES

Research Article

www.acsami.org

Encapsulating $Bi_2Ti_2O_7$ (BTO) with Reduced Graphene Oxide (RGO): An Effective Strategy to Enhance Photocatalytic and Photoelectrocatalytic activity of BTO

Satyajit Gupta[†] and Vaidyanathan (Ravi) Subramanian*[,†]

[†]Department of Chemical and Materials Engineering, University of Nevada, Reno, Nevada 89557, United States

Supporting Information

ABSTRACT: Multimetal oxides ($A_xB_yO_z$) offer a higher degree of freedom compared to single metal oxides (AO_x) in that these oxides facilitate (i) designing nanomaterials with greater stability, (ii) tuning of the optical bandgap, and (iii) promoting visible light absorption. However, all $A_xB_yO_z$ materials such as pyrochlores ($A_2B_2O_7$)—referred to here as band-gap engineered composite oxide nanomaterials or BECONs—are traditionally prone to severe charge recombination at their surface. To alleviate the charge recombination, an effective strategy is to employ reduced graphene oxide (RGO) as a charge separator. The BECON and the RGO with oppositely charged functional groups attached to them can be integrated at the interface by employing a simple electrostatic self-assembly approach. As a case study, the approach is demonstrated using the Pt-free pyrochlore bismuth titanate (BTO) with RGO, and the application of the composite is investigated for the first time. When tested as a photocatalyst toward hydrogen production, an increase of ~250% using BTO in the presence of RGO was observed. Further, photoelectrochemical measurements indicate an enhancement of ~130% in the photocurrent with RGO inclusion. These two results firmly establish the viability of the electrostatic approach and the inclusion of RGO. The merits of the RGO addition is identified as (i) the RGO-assisted improvement in the separation of the photogenerated charges of BTO, (ii) the enhanced utilization of the charges in a photocatalytic process, and (iii) the maintenance of the BTO/RGO structural integrity after repeated use (established through reusability analysis). The success of the self-assembly strategy presented here lays the foundation for developing other forms of BECONs, belonging to perovskites (ABO_3), sillenite ($A_{12}BO_{20}$), or delafossite (ABO_2) groups, hitherto written off due to limited or no photoelectrochemicalactivity.

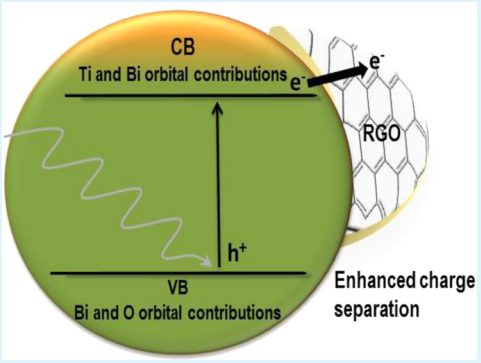

KEYWORDS: *energy conversion, reduced graphene oxide, photoelectrochemical, photocatalysis, semiconductors, bismuth titanate*

1. INTRODUCTION

Hydrogen is a globally recognized clean and eco-friendly energy carrier. The photocatalytic approach to produce hydrogen using two decentralized and perennial resources—water and sun—continues to be a promising but challenging option.[1−5] However, the photocatalytic approach is undeniably the only strategy, to meet the ever increasing global energy needs in a sustainable manner. Oxides have traditionally been the core material of choice due to their multifunctional properties relevant to any photocatalytic process, including hydrogen generation.[6−10] Upon illumination of an appropriate photocatalyst, charged species (electron−hole pairs) required to produce hydrogen are generated. Most members of the oxide semiconductor family of compounds are limited in their ability to facilitate separation of these photogenerated charges. For oxide-based photocatalysis to be practical and commercially viable, it is critical to form nanostructures of oxides with something that (i) aids in the separation of photogenerated charges in real time, (ii) demonstrates universal compatibility with any member of the extended oxide family group such as multimetal oxides, (iii) integrates with oxide easily using a simple approach, (iv) is cost competitive, and (v) enables the oxide to demonstrate improved efficiency in any photodriven applications.

One of the choice additives that meet all of the above criteria is reduced graphene oxide (RGO). Nanocomposites of single metal oxides such as TiO_2, or even nonoxide semiconductors such as Cu_2S that contain RGO as a building block, can significantly and positively impact optical, surface, catalytic, and electronic properties of oxides in ways thought not likely possible, until recently.[11−13] The key to the success of the integration is the ability to leverage the unique transport properties of RGO in the oxide-RGO nanostructures. The beneficial role of RGO addition is clearly evidenced from some leading examples in photocatalytic (conduction and valence band-driven redox reactions),[11] electrochemical (H_2 generation),[12] and photoelectrochemical processes (improvement in the photoelectrochemical response of Cu_2S quantum dots).[13]

Received: May 30, 2014
Accepted: August 1, 2014
Published: August 1, 2014

Furthermore, the multifunctional attributes of RGO in promoting light-activated reactions are also evident through end-user applications such as (i) photocurrent enhancement for solar-cell anodes through strong electronic coupling with TiO_2[14] and (ii) solar fuels such as hydrocarbons[15] or hydrogen.[16]

Among the oxides, unlike the popular single metal oxides (AO_x), multimetal oxides ($A_xB_yO_z$) such as pyrochlores ($A_2B_2O_7$) offer distinct advantages. The chief enabling features of these materials are (i) increased options to form unique formulations by tailoring the choice of elements in the A and B sites (for example, this is evident with the flexible structural formula of pyrochlore), (ii) increased potential for band gap engineering, and (iii) the possibility to achieve materials that demonstrate visible light activity using earth-abundant elements as building blocks.[17] Because of these unique features, we refer to these multimetal oxides as band-gap engineered composite oxide nanostructures or BECONs. The multimetal oxides can be synthesized using simple, cost-effective, and scalable approaches with tight size and dimensional control.[18] Furthermore, as indicated in Scheme 1, designing new

Scheme 1. Relative Energy Levels of the Valence Band and Conduction Band of Various Oxides at pH 7 with Respect to NHE[a]

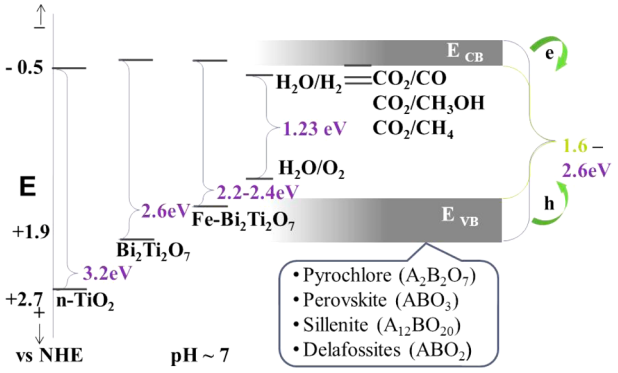

[a]The design of new band gap-engineered composite oxide nanostructures (BECONs) with E_g in the range of 1.6–2.6 eV will promote photocatalytic processes such as water splitting, CO_2 conversion to hydrocarbons, and pollutant remediation.

BECONs can potentially promote synthesis of solar fuels. They need not be limited to hydrogen production alone but can also be used for sustainable green energy technologies such as CO_2 control, hydrocarbon-based fuel production, and energy storage.[19] To enable these features, BECONs with band gap in the region of 1.6–2.8 eV, which is the desired band gap for visible light-driven reactions, are required. The only area multimetal oxides significantly lag behind compared to single metal oxide is the separation of photogenerated charges.[20,21]

The synergistic coupling of RGO in the area of improving photoactivity has generally been explored with single metal oxides as a candidate material. Studies that have focused on TiO_2 of various forms are relatively better understood.[22] With regards to RGO compatibility with nonoxides, MoS_2/RGO-based molecular p–n junction heteroarchitecture has been synthesized and has demonstrated an enhanced charge separation and reduced charge recombination.[23] That system also improved the photocatalytic hydrogen generation as compared to pure MoS_2. In another example, α-Bi_2O_3 microneedles hybridized with graphene oxide (GO) also showed better photocatalytic activity.[24]

In the context of the work presented here, it is noteworthy to mention that bismuth-based oxides are the focus of this study since Bi is a nontoxic source and is known to promote visible-light absorbance.[25] However, to the best of our knowledge the impact of RGO in the photoelectrocatalytic and activity of bismuth titanate (BTO) has not yet been investigated. BTO is a pyrochlore-type multifunctional photocatalyst that facilitates light-driven processes such as solar-fuel generation and dye degradation.[26] Compared to TiO_2 (band gap or E_g of 3.2 eV), BTO has a lower optical band gap (E_g of 2.8 eV). Therefore, absorption spectra of BTO show a red shift compared to TiO_2. In an earlier modeling analysis, we thoroughly investigated the structure–activity relationship of BTO using pseudopotential plane wave calculations and partial density of states (PDOS).[17] Unfortunately, in such semiconductor systems, the recombination of photoilluminated charges [electron (e^-) and hole pair (h^+)] causes a detrimental effect in the photoactivity. The prolonging of the separation among photogenerated charges is critical for the enhancement of photoactivity.

The present work delineates the self-assembly of a two-dimensional RGO with zero-dimensional BTO nanoparticles to form a nanocomposite (rGBTO). Specifically, a simple ligand chemistry-based electrostatic approach to synergistically couple RGO with BTO is presented, and the features of the composite thus obtained are examined using complementary characterization tools. Not only is the hydrogen yield enhanced in the presence of RGO, repeated runs indicate the stability of the RGO/BTO composite, highlighting its sustainable use. Furthermore, photoelectrochemical measurements offer insights into the charge-transport properties at the composite interface. The representative case study presented here reveals a unique approach to effectively integrate a BECON with RGO and demonstrates the viability of the composite to drive photoelectrocatalytic processes. The findings reported in this work are expected to aid in the synthesis strategy of other BECONs that belong to family groups such as perovskites (ABO_3), sillenite ($A_{12}BO_{20}$), or delafossite (ABO_2) configurations (besides pyrochlores), and to build upon this concept for the sustainable promotion of photodriven applications.

2. EXPERIMENTAL SECTION

2.1. Chemicals. Bismuth(III) nitratepentahydrate was used as a precursor and was obtained from Alfa Aesar. Titanium(IV) isopropoxide (97%), terpenol, and aminopropyltrimethoxysilane (APTMS) were obtained from Sigma-Aldrich (St. Luis MO). Nitric acid, sulfuric acid (ACS, BDH3046–2.5LPC, 68%), and ammonia solution (A667–212, ≥25%) were obtained from BDH Aristar and Fisher Scientific. Graphite powder was obtained from Bay Carbon (SP-1). Acetic acid (CH_3COOH), potassium permanganate ($KMnO_4$), and sodium nitrate ($NaNO_3$) were obtained from EMD Chemicals. Ethanol (CH_3CH_2OH) and methanol (CH_3OH) were obtained from Pharmco-Aaper. The chemicals were used without any further purification. Ultra high-purity deionized water (Millipore system) was used for the synthesis. The ammonia and the nitrogen gas cylinders were obtained from Airgas (99.99%).

2.2. Syntheses. *2.2.1. Synthesis of Bismuth Titanate Nanoparticle.* The BTO nanoparticles were synthesized by a co-precipitation method, followed by furnace treatment. The synthetic protocol is described in detail in the Supporting Information (Section 1), and the process schematic is shown in Figure S1.

2.2.2. Synthesis of Amine-Functionalized Bismuth Titanate. The as-prepared BTO (1 g) nanoparticles were dispersed in dry ethanol (150 mL) by ultrasonication to ensure uniform dispersion. Amino-

Scheme 2. Step-by-Step Procedure to Couple GO and BTO Using Ligand Chemistry and Electrostatic Self-Assembly Approach, Forming a Composite Nanostructure, Referred to Here as rGBTO, after Thermal Treatment

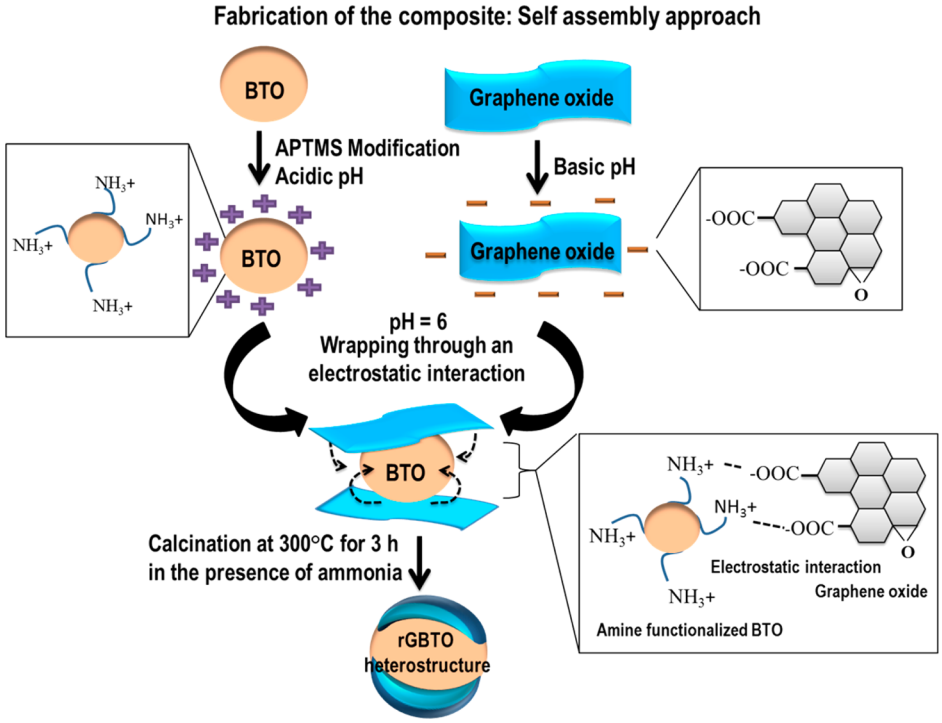

propyltrimethoxysilane (APTMS) was added in a ratio of 0.19 mmol mL^{-1} and refluxed for 20 h under a N_2 atmosphere. Subsequently, the mixture was cooled to room temperature, and the powder was separated by centrifugation. The powder was washed several times with ethanol to remove any unreacted APTMS. Finally, it was dried at 80 °C in an oven and stored for further use.

2.2.3. Synthesis of Graphene Oxide. GO was synthesized by the modified Hummer's method.[27] The synthetic method is discussed in the Supporting Information (Section 2).

2.2.4. Synthesis of rGBTO Nanostructures. A "self-assembly" method, well-documented in the literature,[28−37] was used to fabricate the reduced rGBTO nanostructures. First, GO was dispersed in water, and the pH was maintained at ∼8 using ammonium hydroxide. The basic medium aids in the deprotonation of the carboxylate groups resulting in the GO becoming negatively charged (Scheme 2). The amine-functionalized BTO nanoparticles were separately dispersed in water, and the pH was maintained at ∼3 by the addition of acetic acid. This makes the surface positively charged. Then various amounts (0.25, 0.75, 1, and 6 wt %) of GO suspension (with respect to BTO) were added to the BTO dispersion. These composites are denoted as rGBTO0.25, rGBTO0.75, rGBTO1, and rGBTO6. The ratio of the photocatalyst and reduced graphene oxide BTO/RGO in the composite catalysts are thus pristine BTO, 1:0; rGBTO0.25, 1:0.0025; rGBTO0.75, 1:0.0075; rGBTO1, 1:0.01; and rGBTO6, 1:0.06. The addition causes an immediate flocculation due to assembly of oppositely charged components and also results in a transparent solution. Beyond 1 wt %, the solution does not remain transparent but gives a brown color due to excess graphene oxide. The flocculated matrix was separated using centrifugation, dried, and annealed under constant flow of ammonia at 300 °C for 3 h (inside a tube furnace obtained from Lindberg Bluebox furnace-Thermo Fisher Scientific). This process results in the formation of the rGBTO composites. The thermally induced reduction of GO[38] was carried out at a temperature chosen from the observations in the thermogravimetric analysis (TGA) (the temperature was chosen where the weight loss achieves a steady state).

A control experiment was also carried out using pristine and nonfunctionalized BTO, following the procedure mentioned above (using 1 wt % of GO with respect to BTO). In this case, no flocculation was observed. However, the mixture was separated by centrifugation, dried, and annealed in an ammonia atmosphere. The sample was termed S1. In addition, another composite sample was prepared using 1 wt % of GO by solid-state mixing followed by annealing in ammonia atmosphere. This sample was labeled S2.

2.3. Characterization. *2.3.1. Surface and Optical Characterization.* The phase analysis of the synthesized photocatalysts was carried out using X-ray diffraction (XRD) [Philips model 12045 B/3X-ray diffractometer with a scan rate of 0.03° min^{-1}]. A Hitachi S-4700 scanning electron microscope (SEM) was used to determine the morphology of the as-synthesized BTO powder and the composites. A JEOL 2100F high-resolution transmission electron microscope (HRTEM) was used to examine the rGBTO composite. The BTO and rGBTO were dispersed in ethanol and drop-casted over carbon tape (purchased from Ted Pella). The morphologies of the particles were observed under an accelerating voltage of 3 kV. TGA was performed using a PerkinElmer STA 6000 (simultaneous thermal analyzer) with an alumina crucible under nitrogen flow at a heating rate of 5 °C min^{-1} (flow rate of 20 mL min^{-1} was used). The absorption properties and band gap of the powder were examined using a UV−visible spectrophotometer (Shimadzu UV-2501PC) over a wavelength region of 300−800 nm. Fourier transform infrared (FTIR) analysis of the samples was performed using Thermo Nicolet 6700 spectrophotometer in the range from 400 to 4000 cm^{-1} (in transmittance mode). Micro-Raman spectroscopies of the samples were carried out using a ReinshawinVia microscope at room temperature with a 633 nm laser under low laser intensities (to avoid sample heating/burning). The spectra were collected by averaging multiple scans. X-ray photoelectron spectroscopy (XPS) was recorded using PHI 5000 Versa Probe System, Physical Electronics, MN, and the C_{1s} peak was used as a reference to calibrate the binding energies. Photoluminescence (PL) spectra of the samples were measured using Fluoromax-3 Horiba Fluorimeter.

2.3.2. Photoelectrochemical Characterization. The current−voltage (I−V) characteristics of the catalysts were measured using a three-electrode system, with a quartz cell and a Pt wire as the counter electrode, and a leak-free Ag/AgCl (in 3 M KCl) as the reference electrode. A 0.5 M NaOH solution in water was used as the electrolyte. An Autolab PGSTAT 30 electrochemical analyzer was used for the

photoelectrochemical analysis. The working electrode (catalyst-deposited conducting glass slide; the method of the film preparation is discussed in Supporting Information, Section 3) was irradiated with a 500 W Newport xenon lamp as the light source with a light intensity of ~100 mW cm^{-2} with 0.5 M $CuSO_4$ solution as a far-UV cutoff filter. The electrochemical impedance of the catalyst samples were performed using a Gamry electrochemical workstation in a three-electrode apparatus. The ITO deposited with the catalysts served as the working electrode, with a platinum wire as the counter electrode, and Ag/AgCl (saturated KCl) as the reference electrode. The measurement was performed in the presence of a 0.2 M Na_2SO_4 solution under dark and illuminated conditions.

2.3.3. Photocatalytic Slurry Reactor for the H_2 Evaluation. An off-the-shelf slurry reaction system was used to perform the photocatalysis experiments. The H_2 yield estimation was carried out by employing a method that involved the use of a slurry reactor connected with a high-pressure immersion-type medium-pressure quartz mercury lamp (Section 4, Figure S2, Supporting Information). The detail of this experiment is given in the Supporting Information (Section 4).

3. RESULTS AND DISCUSSION

3.1. Characterization of Graphene Oxide. The synthesized GO and its transformation to RGO was characterized using TGA. These results are shown in Figure 1. The TGA of

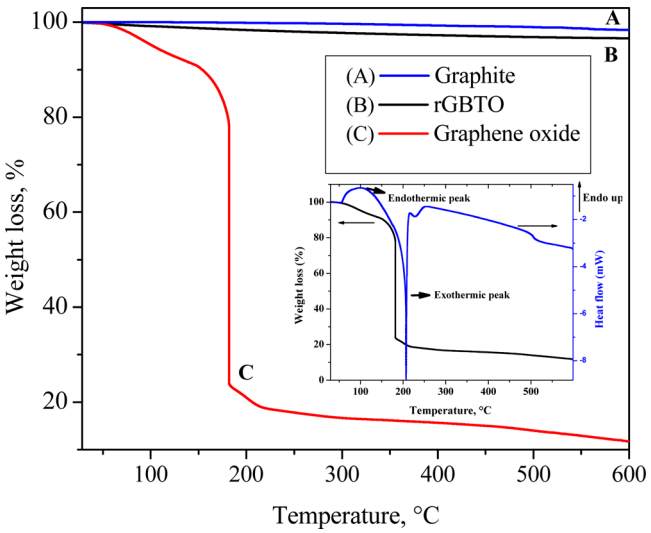

Figure 1. Thermogravimetric analysis (TGA) of (A) pristine graphite, (B) reduced graphene oxide + BTO (rGBTO), and (C) graphene oxide (GO) are shown. The XYY plot in the inset shows the TGA and differential thermal analysis (DTA) data of the GO.

the base material graphite is also shown (Figure 1A). No weight loss in the temperature range from 30 to 350 °C is observed. However, in the case of GO, the initial weight loss of ~10%, from 30 to 150 °C, is noted. This is attributed to the removal of physisorbed water at the GO surface [also indicated by an endothermic peak in the differential thermal analysis (DTA) curve, Figure 1 inset]. From 150 to 300 °C a significant weight loss of ~68.5% was observed with a strong exothermic peak at ~200 °C in the DTA curve (Figure 1 inset). A majority of the weight loss is noted as a sharp fall in the curve at a temperature of ~185 °C. This observation can be attributed to the pyrolysis of the various functional groups such as hydroxyl, epoxy, and carboxylate. During the pyrolysis process, weight loss occurs via these functionalities generating carbon monoxide (CO), carbon dioxide (CO_2), and moisture (H_2O).[39] After 300 °C, the weight remains almost constant. The formations of these groups were further characterized by FTIR spectroscopic technique.

The FTIR spectra of neat graphite precursor and the product formed from it are shown in Supporting Information, Figure S3. The spectrum of graphite does not indicate any features in the wavenumber window of 3500−500 cm^{-1}, while several features are observed in this region after the oxidative treatment of graphite. These features are attributed to the formation of different functional groups. The key peaks are identified as follows: a broad peak around 3120 cm^{-1} is attributed to hydroxyl (−OH) stretching, and the 1620 cm^{-1} peak is due to −OH bending or in-plane vibrations of sp^2-hybridized C═C bonding (Supporting Information, Figure S3).[40] A peak around 2760 cm^{-1} is due to aliphatic C−H stretching, whereas peaks observed around 1724 cm^{-1}, 1221 cm^{-1}, and 1042 cm^{-1} are due to the presence of carbonyl (−C═O), −C−OH stretching, and epoxy (C−O−C)-containing functionalities, respectively.[41] These peaks indicate the formation of GO. The as-synthesized sample at this stage is readily dispersible in water due to the polar functionalities at the surface. Thus, the FTIR observation supports the TGA results in that the weight loss observed from 120 to 300 °C in TGA is caused by the loss of the functionalities identified using FTIR.

3.2. Characterization of Surface-Modified BTO. The surface functionalization of BTO was also tracked using FTIR spectroscopy, as indicated in Supporting Information, Figure S4. It can be observed that after functionalization, additional peaks appear, which are attributed to the surface modification by APTMS. In pristine BTO, the broad peak at 3264 cm^{-1} is due to −OH groups on the nanoparticle surface, and the peak at 1641 cm^{-1} is due to the −OH bending vibrations. After APTMS treatment, new peaks appear at 2918 and 2846 cm^{-1}. These are characteristic of asymmetric and symmetric $-CH_2$ stretching vibrations, respectively.[42] The appearance of a band at 1470 cm^{-1} is attributed to the $-CH_2$ bending (scissoring) vibration. The band appearing at 1562 cm^{-1} is caused by the N−H bending (scissoring), the band at 1130 cm^{-1} is due to C−N stretching, and the peak at 1035 cm^{-1} is due to (M−O−Si) stretching (where M-surface metal from BTO). The chemistry of the surface functionalization process of the BTO before it is made to interact with the RGO is shown in Supporting Information, Figure S4 (inset).

3.3. Characterization of the GO/BTO Composite after Thermal Treatment. *3.3.1. Structural Characterization Using FTIR.* The FTIR of BTO and GO (1 wt %) with BTO after thermal treatment is shown in the Supporting Information, Figure S5. After thermal treatment, a significant reduction in the −OH and carbonyl peak intensity (1720 cm^{-1}) can be noted. Two key observations are important here. First, the carbonyl peak totally disappears after heat treatment. The other peaks, except the peak at 1042 cm^{-1} (epoxy functionality), are also removed. This is because of the partial recovery of graphene structure. Second, the occurrence of a new peak at ~1569 cm^{-1} is due to the skeletal vibration of the graphene sheet. This observation also alludes to a partial recovery of the sp^2 framework. It is known that a two-step chemical exfoliation followed by thermal treatment leads to the transformation of graphite to RGO. FTIR measurements aid in the tracking of graphite-to-RGO transformation by monitoring the evolution of skeletal vibrations, characteristic of graphene-like behavior of the RGO.[43−45] These two observations indicate the formation of reduced graphene oxide (RGO) from

graphene oxide. The composite nanostructure after thermal treatment is referred as rGBTO.

3.3.2. Structural Characterization Using TGA. The TGA thermogram of rGBTO is showed in Figure 1B. As expected, the result indicates an insignificant weight loss in the temperature range of 30−600 °C, implying the fact the GO was converted to a graphene-like structure by losing most of the surface functionalities during the thermal annealing process. This result is complemented by the FTIR analysis as well (discussed earlier), which indicates that the GO-to-RGO transition occurs during the thermal treatment after the electrostatic interaction (see Experimental Section and Supporting Information).

3.3.3. Structural Characterization Using Raman. The product of thermal treatment of the rGBTO and GO was further investigated using Raman spectroscopy and is shown in the Supporting Information, Figure S6. The two peaks observed at 1352 and 1589 cm^{-1} are attributed to the D band (defect-mediated breathing mode of A_{1g} symmetry) and G band (first-order scattering of the E_{2g} mode), respectively. Alternately, the I_D/I_G ratio was observed to be 0.76 for GO; it increases to 0.85 for the thermally treated rGBTO. The increase in the I_D/I_G ratio is attributed to the formation of smaller sp^2 domains during the thermal treatment process.[41,46,47] In addition, a downshift of G bands from 1592 cm^{-1} (GO) to 1584 cm^{-1} (rGBTO) was observed after thermal reduction, indicating the formation of more graphene domains.[48] Thus, the combination of the results obtained using FTIR and Raman reveals that during the thermal treatment of the BTO−GO composite prepared by electrostatic assembly, GO was converted to RGO.

3.3.4. Structural Characterization Using XPS. To further probe the interface of the BTO−RGO material, XPS analysis was performed. The C_{1s} feature of GO is shown in Supporting Information, Figure S7A. The deconvolution of this broad asymmetric feature shows two peaks, specifically, a peak at 284.4 eV, which corresponds to graphitic −C−C, and a relatively high-intensity peak at ∼287 eV, which corresponds to −C−O functionalities, formed during the oxidation process.

The deconvolution of C_{1s} of RGO is shown in Supporting Information, Figure S7B. This indicates that the shape of the peak totally changes after the thermal treatment with a reduction in the higher binding energy peak at 287 eV. The deconvoluted peaks can be designated as (a) graphitic −C−C (284.4 eV), (b) −C−N (285.9),[48] (c) −C═N (287 eV),[48] (d) −O−C═O (288.5 eV),[41,49] and (e) $\pi-\pi^*$ shakeup satellite peak (290.6 eV).[50] The occurrence of −O−C═O indicates the formation of Ti−O−C═O by the condensation of surface Ti−OH of BTO and COOH groups at the graphene surface.[41,49]

The nitrogen doping in the RGO is also evident from XPS studies (Supporting Information, Figure S8). The analysis showed a broad asymmetric peak around 400 eV (N 1s), which corresponds to the doped nitrogen in the RGO matrix.[38]

3.3.5. Phase and Morphological Characterization Using XRD, SEM, and TEM. The phase analysis of the as-synthesized pristine BTO and of the BTO with RGO was performed using XRD and is reported in Figure 2. The peaks in the XRD correspond to the pyrochlore-phase of the BTO. The detailed characterization of this phase is presented elsewhere.[26] The XRD peaks are indexed as per JCPDS Card No. 32−0118, where the peak at 28.7° corresponds to the (622) *hkl* plane, while 29.9° corresponds to the (444) *hkl* plane. The latter is the highest intensity peak unique to the composite and is also

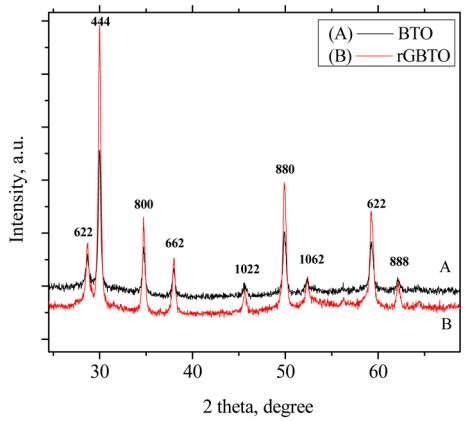

Figure 2. X-ray diffraction (XRD) patterns of the (A) BTO and the (B) BTO wrapped in RGO (rGBTO) are shown. The various peaks corresponding to the BTO phase are indexed in both samples.

present in the samples with the RGO. This observation indicates that the physical integrity of the BTO is maintained when it is synthesized as a composite with RGO.

The SEM was used to analyze the physical features of the pristine BTO and the rGBTO samples. The pristine BTO showed a particle size of 30 ± 10 nm [Figure 3A]. The evolution of the rGBTO composite with an increasing amount of GO addition is shown in the collage of images in Figure 3B−D. The difference between Figure 3A and the rest of the SEM images in Figure 3 is that the overall size of the composite is increased irrespective of the GO content. This observation indicates that the electrostatic self-assembly approach results in the BTO encapsulation. Such a close contact between RGO sheets and the BTO surface is desirable for the reasons identified in the Introduction and is expected to assist in the photocatalysis (discussed later). To further understand the microstructure, TEM analysis of the composite nanostructure was performed. The TEM image in Figure 3E indicates the presence of RGO sheet encapsulating one or more of the BTO nanoparticles. The RGO and the BTO are labeled in the Figure. Such a composite structure formation (inorganic oxide with graphene or graphene-like material) is observed in related studies.[51−53] Thus, in conjunction with SEM, TEM aids in further understanding the BTO/RGO composite nanostructure formation.

The continued existence of a fairly dispersed BTO particle presence with increased GO content leads to an interesting observation. With the increase in the loading of RGO, it is possible that the GO exists as multiple layers wrapped around the already coated BTO. As the synthesis method followed here is an electrostatic self-assembly approach, this form of wrapping can be expected to continue until the charge neutralization point between positively charged (+Ve) BTO surface and negatively charged (−Ve) GO is reached. In the case of high GO loading, the excess GO is expected to remain in the solution and cannot wrap around the BTO surface through electrostatic interaction, due to lack of any positively charged surface (Supporting Information, Figure S9).

4. PHOTOCATALYTIC HYDROGEN GENERATION

4.1. Boosting the Hydrogen Yield. The photocatalytic hydrogen-generation studies using the composite nanostructures were carried out in a slurry reactor setup as described in Supporting Information (Section 4 and ref 26). It can be

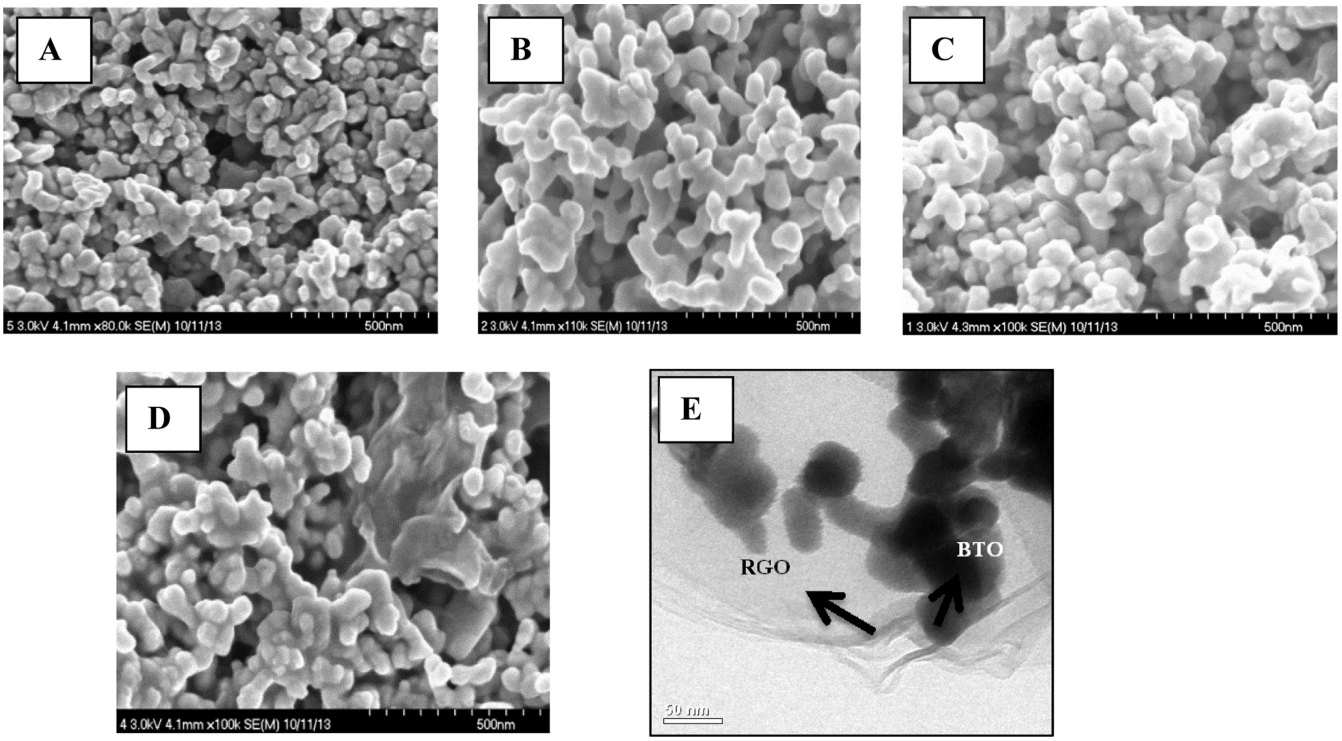

Figure 3. A series of microscope (SEM) images of the synthesized (A) BTO [no RGO], (B) rGBTO0.75 [RGO = 0.75 wt %], (C) rGBTO1 [RGO = 1 wt %], and (D) rGBTO6 [RGO = 6 wt %]. The TEM image of rGBTO composite is shown in (E).

observed from Figure 4 that the presence of RGO (rGBTO) shows a gradual increase in the overall hydrogen yield

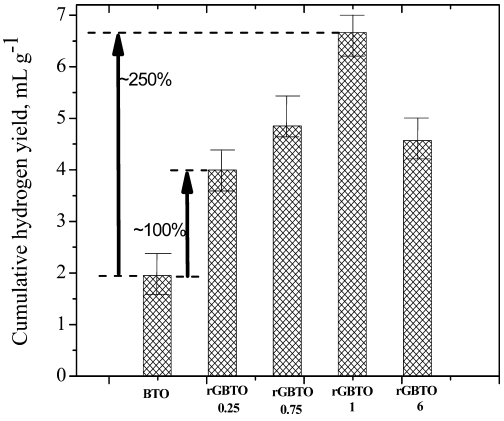

Figure 4. Cumulative hydrogen yield obtained using the pristine BTO and the BTO/RGO composite catalysts with RGO content varied from 0.25 to 6 wt %. The results presented in this bar graph are obtained in the presence of a water/methanol mixture with 250/50 (v/v) composition and UV−vis illumination continuously over a period of 130 min.

compared to the pristine BTO. On comparing the activity of BTO and 0.25 wt % RGO-loaded BTO, an ∼100% increase in the hydrogen yield is noted. Note that the color of the photocatalyst becomes darker when the RGO loading is increased, as indicated in Figure 5. The hydrogen yield continues to gradually increase further until a loading of 1 wt % rGBTO is reached. The 1 wt % RGO-loaded BTO shows an ∼250% increase in the hydrogen yield compared to the pristine BTO, highlighting the benefits of RGO inclusion.

However, a further increase in the RGO loading beyond the 1 wt % indicates a decrease in the hydrogen yield as evidenced from the results of the 6 wt % sample. This observation can be attributed to the light shielding effect of the RGO. With the increase in the graphene-like material (such as RGO) loading, the RGO at the surface can block the light absorption and reduce the light intensity at the surface resulting in a reduced photocatalytic activity.[54,55] Further, the excess RGO can block the active sites of the catalyst. This effect can also contribute toward the activity reduction.[56] This phenomenon is responsible for driving down the performance of the photocatalyst. Thus, the reason for the 250% increase in the performance with the 1 wt % rGBTO composite is (i) the achieving of an optimal conjugation of RGO with the BTO and (ii) RGO-driven enhanced separation of photogenerated charges. The proof for the latter aspect is further evidenced using the photoelectrochemical measurements (discussed in Section 5.2).

We also conducted two experiments as control. First, hydrogen generation from pristine BTO with pure water using the photocatalytic reactor and UV−visible illumination was performed. This experiment showed no hydrogen generation during the entire course of the photocatalytic reaction. Second, we also carried out another reaction with APTMS-modified BTO after thermal treatment at 300 °C. (The condition used for the synthesis was maintained the same as the one used for the composite catalysts, i.e., rGBTO.) The thermally treated APTMS-modified BTO did not produce any hydrogen during the photocatalytic reaction from pure water. The absence of hydrogen in these two experiments shows that no photocatalytic or APTMS degradation-related hydrogen generation occurs in the control reaction.

4.2. Mechanistic Insights into Methanol-Assisted H_2 Evolution. The time-resolved hydrogen yield using the BTO

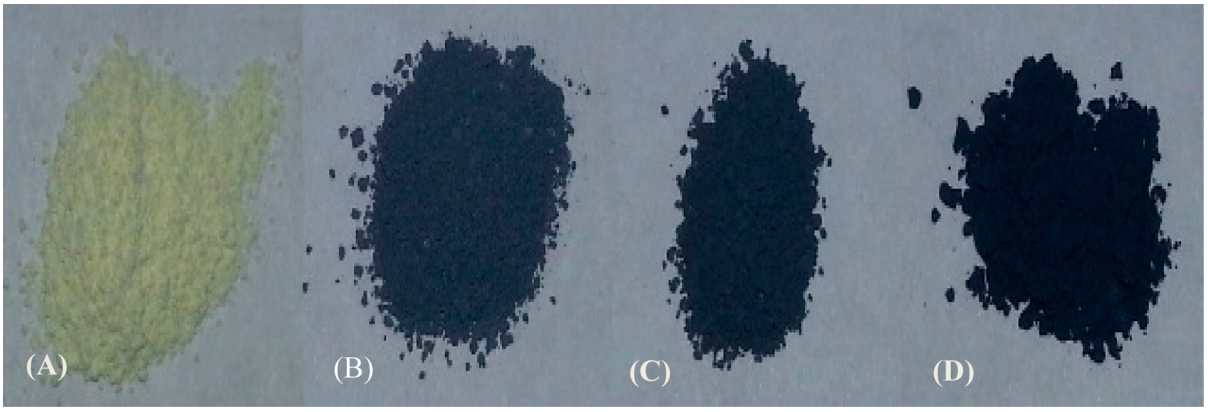

Figure 5. Photographs of the as-synthesized (A) BTO [no RGO], (B) rGBTO0.75 [RGO = 0.75 wt %], (C) rGBTO1 [RGO = 1 wt %], and (D) rGBTO6 [RGO = 6 wt %].

and BTO/RGO composite is shown in Supporting Information, Figure S10. The first 1 h results in a low hydrogen generation. A rapid increase in hydrogen yield is noted between 1 and 2 h. The mechanism of the hydrogen evolution begins with the photogenerated species formation. In the course of the photoillumination, the BTO first generates electron−hole pair (eq 1). The well-known conductive nature of the RGO is responsible for the electrons to move away from the BTO (eq 2). The hole oxidizes the methanol to formaldehyde (dissociation energy of 47.8 kJ mol^{-1}) and generates two protons (eq 3). The photogenerated electrons carried away by the encapsulating RGO (interfacial charge transfer) remain over the carbon network where the two protons react with the electrons (e^-) to generate hydrogen (eq 4). The formaldehyde further oxidizes to formic acid (eq 5), releasing a single proton [H^+]. This formic acid, having a low dissociation energy (−95.8 kJ mol^{-1}), is responsible for the increased rate of hydrogen production at the end of 1 h. At the beginning of the first hour, the formaldehyde builds up as an intermediate of methanol oxidation. When a sufficient amount of formaldehyde is present in the system, its oxidation to formic acid supersedes methanol oxidation rates. This yields a higher rate of hydrogen evolution as evident from the time-resolved data between 1 and 2 h.

The steps involved in the photocatalytic oxidation process can be summarized as follows:[57]

$$\text{rGBTO} \xrightarrow{\text{UV-vis}} e^-_{CB} + h^+_{VB} \quad (1)$$

$$e^-_{CB} \rightarrow e^-_{CB}(\text{RGO}) \quad (2)$$

$$CH_3OH + h^+ \rightarrow HCHO + 2[H^+] \quad (3)$$

$$2[H^+] + 2e^- \rightarrow H_2(g)\uparrow \quad (4)$$

$$HCHO + 2h^+ + 2e^- + H_2O \rightarrow HCOOH + H_{2g}\uparrow \quad (5)$$

$$HCOOH + 2h^+ + 2e^- \rightarrow CO_{2g} + H_{2g}\uparrow \quad (6)$$

To further understand the effects of the intermediates of methanol oxidation and their role, two experiments were carried out. First, the photocatalysts were separated after a 2.1 h run by centrifugation, and FTIR analysis was carried out (Supporting Information, Figure S11). After photocatalytic reaction, the peak noted at 1727 cm^{-1} is attributable to the carbonyl (−C═O) stretching frequency. This is indicative of methanol oxidation resulting in the formation of formaldehyde and formic acid. The other peaks arising at ∼2927, 1387, and 1219 cm^{-1} are due to the $-CH_3$ stretching of adsorbed $-OCH_3$, the −C−H vibration of formic acid and −CO−OH stretching vibration of formic acid,[58] respectively. Thus, the FTIR analysis shows the presence of oxidation products as the factor that influences the rate of hydrogen evolution. Second, since it is reported[57,59] that formic acid and formaldehyde are the byproducts of the oxidation, we performed a set of experiments with formic acid−water and formaldehyde−water as the starting solution (with rGBTO0.75 as the photocatalyst). We ensured that the v/v ratio is the same as methanol−water in both cases. The comparative hydrogen yields from these three mixtures are shown in the bar graph (Figure 6). The hydrogen

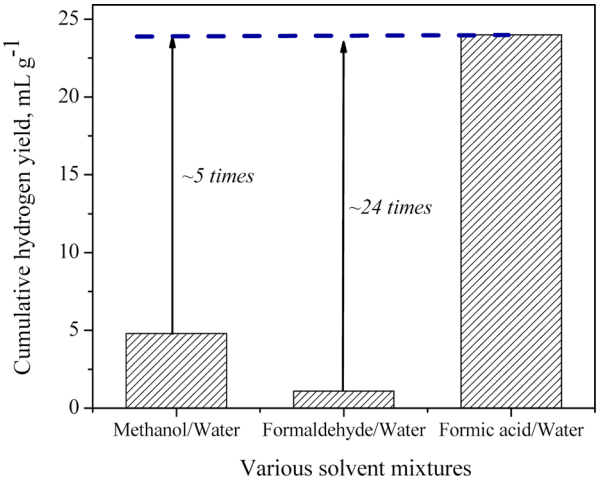

Figure 6. A comparison of the hydrogen yield from various aquous mixtures indicates that the presence of formic acid results in enhanced hydrogen generation.

yield with $HCOOH/H_2O$ is ∼5 times higher than that with methanol/water and ∼24 times higher than that with $HCHO/H_2O$. The fact that the hydrogen yield is highest with formic acid indicates that its presence accelerated the rate of hydrogen production. This experiment, along with the references, confirms that the formation of formic acid as a byproduct of methanol oxidation is the basis for the higher rate of hydrogen evolution.

4.3. Reusability of the Catalyst. To verify the reusability and stability of the composite catalyst, a cycling experiment was performed with the optimal rGBTO1 as well as with rGBTO6.

This experiment was carried out for a prolonged period of time (~8.6 h) under continuous illumination. The results are shown in Figure 7. The cycling experiment indicates a small reduction

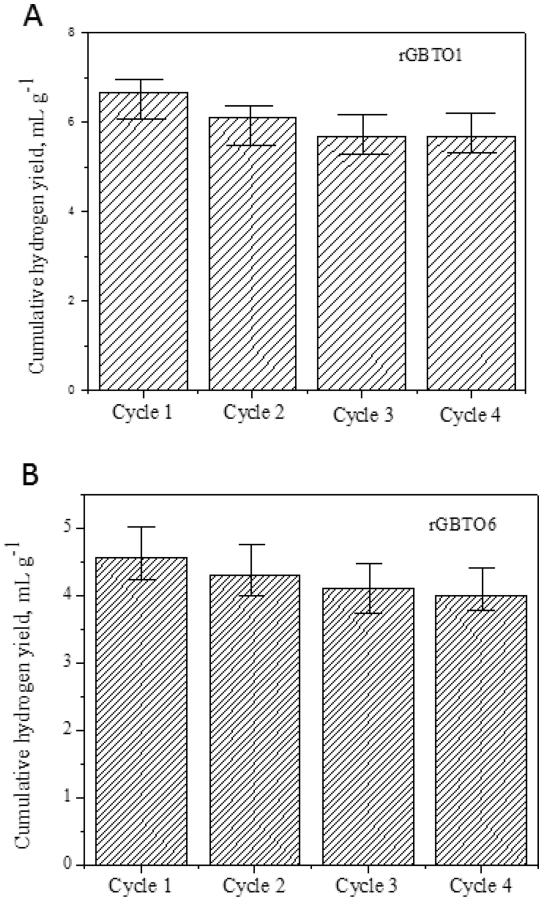

Figure 7. This bar graph shows the reusability characteristics of the RGO/BTO composite photocatalyst with RGO content of (A) 1 wt % (rGBTO1) and (B) 6 wt % (rGBTO6) performed under continuous photoillumination for 8.6 h. The result indicates the stable hydrogen yield at the end of the fourth cycle.

(for rGBTO1) in the cumulative hydrogen over a 2 h run after the first cycle. This reduction of ~10% in the hydrogen yield compared to the first cycle was evident with two batches of samples. The cumulative yield remains constant from the second cycle to the fourth cycle. These results confirm the reusability of the photocatalyst.

It is possible that the intermediates of the reaction could be playing a role in the performance of the catalyst. To evaluate this possibility, FTIR analysis of the used photocatalyst was performed. At the end of the first cycle the used photocatalyst indicates the presence of adsorbed methoxy ($-OCH_3$), carbonyl ($-C{=}O$), and aliphatic groups at the photocatalyst surface. These groups are generated during the catalytic oxidation of methanol as discussed above. The surface coverage by methoxy ($-OCH_3$) and other functional groups such as carbonyl reduces the active sites of BTO, thus hindering the reaction of subsequent methanol molecules at the surface. The presence of these groups is identified as the cause of the observed ~10% decrease in the hydrogen yield. After the second, third, and fourth cycles, almost no reduction was observed, indicating that the photocatalyst is stable. The reason for this no reduction taking place after the second cycle lies in the steric hindrance created by the already adsorbed groups. These groups do not allow blockage in subsequent cycles. The stability of the composite is also attributed to the wrapped RGO around the BTO surface, acting as a protective/passivation layer. The results of Supporting Information, Figure S12 further prove that a simple additive approach to assemble BTO and RGO together does not result in hydrogen yields greater than the electrostatic assembly technique.

5. INSIGHTS INTO THE UNIQUE PERFORMANCE OF THE BTO–RGO COMPOSITE

5.1. Photoelectrochemical Analysis: Current–Voltage Response of the BTO/RGO Films. Photoelectrochemical measurements were performed to test the hypothesis that the presence of RGO will promote charge separation. The current–voltage (I–V) characteristics of the nanostructures were measured using the film of the catalysts deposited over the conducting glass slides. The typical I–V responses of the films are shown in Figure 8A. The rGBTO1 sample [$I_{(at,\ V=0)}$ = 41 μA] showed a better current response under AM 1.5 illumination (intensity 100 mW cm^{-2}) light condition. Compared to this result, the response of the BTO samples

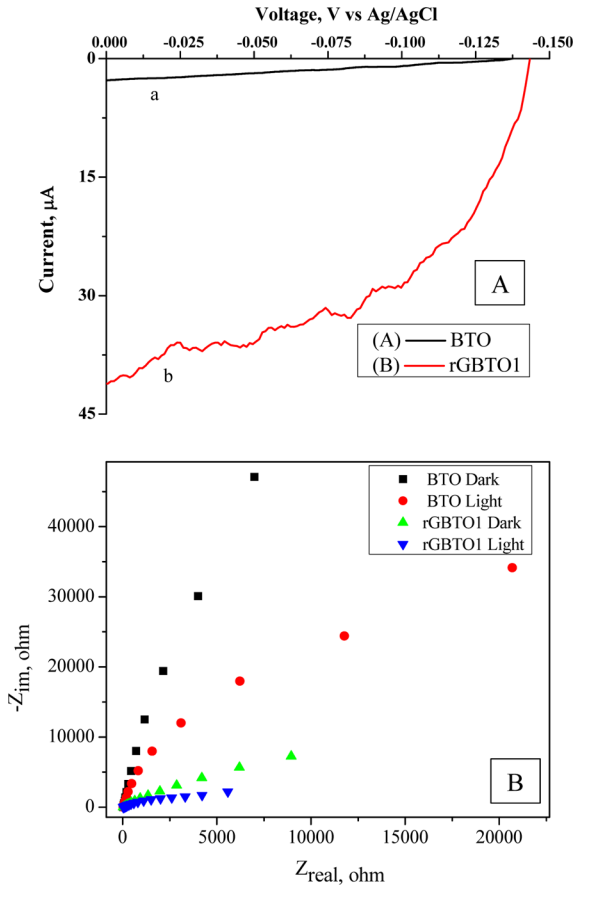

Figure 8. (A) The photoelectrochemical response of the (a) BTO and (b) RGO/BTO nanostructures with 1 wt % RGO was examined using I/V measurements. The experiment was conducted in a three-arm photoelectrochemical cell with the photocatalyst film as the working electrode and aqueous 0.5 M NaOH solution as the electrolyte in the presence of AM 1.5 (100 mW/cm^2) illumination. (The films were prepared from a terpenol-based solution on ITO/glass slides). (B) The electrochemical impedance response of BTO and RGO/BTO nanostructures under dark and illuminated condition.

dx.doi.org/10.1021/am503396r | ACS Appl. Mater. Interfaces 2014, 6, 18597–18608

were rather insignificant. (BTO displayed a photocurrent of $I_{(at,\ V=0)}$ = 2.8 μA under the same condition).

The higher current generation/better photoresponse from rGBTO samples demonstrates that the presence of the RGO indeed facilitates electron removal and transport (immediately upon generation in the BTO) compared to pristine BTO. This photoelectrochemical study complements the photocatalytic results in that the improved charge separation and electron transport allows for greater hole availability to promote oxidation reactions, consistent with the hydrogen evolution results made with rGBTO earlier [Figure 4]. Furthermore, a negative shift in the apparent flat band potential of the films with 1 wt % rGBTO compared to the BTO film is noted. This shift indicates an electron accumulation in the rGBTO film. This is also evidence that the holes produced upon illumination are not consumed by recombination, since electron accumulation gives rise to this shift. Instead the holes are available for photocatalytic hydrogen generation, as again indicated in the mechanism and the results of Figure 4.

5.2. Electrochemical Impedance Analysis. Electrochemical impedance analyses were performed to understand the charge-transfer mechanism in the BTO and rGBTO composite systems. In an electrochemical impedance response, the radius of arc reflects the effectiveness of charge transfer occurring in the system. Summarily, the smaller the radius of arc, the more effective is the charge transfer occurring within the system.[28,60−62] Electrochemical impedance analysis (Figure 8B) shows that there is a decrease in the radius of the arc in the rGBTO composite compared to BTO samples when tested under dark and illuminated conditions. This observation indicates that an efficient separation of electron−hole pairs occurs in the presence of RGO. The inference drawn from PL analysis (discussed below) also complements this inference drawn from EIS measurements.

5.3. Photoluminescence Analysis. Photoluminescence (PL) measurements were performed to observe the effect of RGO inclusion on the electron−hole recombination in the BTO and rGBTO. From Figure 9 it can be observed that the PL intensity from BTO is caused by the recombination of electron−holes in the BTO. The PL intensity is significantly reduced with rGBTO compared to the pristine BTO. This is because the excited electrons are delocalized in the RGO sheet and are not consumed by recombination. The role of RGO in promoting the separation of photogenerated electrons is thus evident. This approach to determine charge separation is documented elsewhere as well.[49,63] This reduced recombination was the basis for the observed enhancement in the photocatalytic activity of the rGBTO.

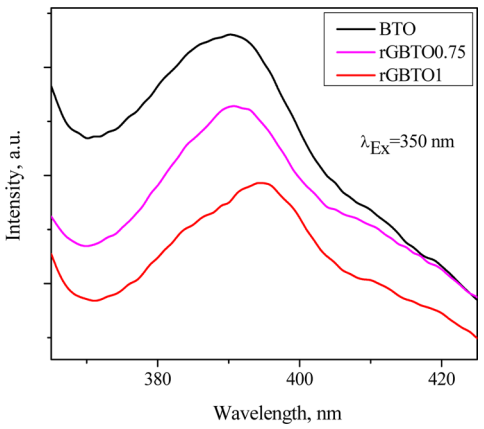

Figure 9. Photoluminescence spectra of BTO and rGBTO composites (rGBTO0.75 and rGBTO1). The measurements were performed using an excitation beam (λ_{ex} = 350 nm) with the photocatalysts.

5.4. UV−Visible Analysis: Extended Light Absorption of the Composites. The UV−visible absorption spectra of the composites with various RGO content is shown in Figure 10.

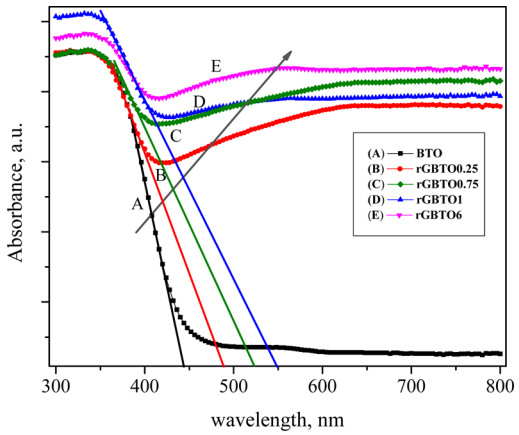

Figure 10. UV−visible spectra of the pristine BTO and the rGBTO composites with RGO content varied from (A) 0 wt %, (B) 0.25 wt %, (C) 0.75 wt %, (D) 1 wt %, and (E) 6 wt % shows a red shift in the optical absorbance onset from 444 to 547 nm.

Because of the opaque nature of the composites, diffuse reflectance measurements were performed and later transformed. BTO exhibits an absorption onset at ∼444 nm. This onset is attributed to the Bi, which causes the valence band to shift closer to the conduction band.[26] With an increase in the RGO content there is a progressive red shift in the absorbance onset. In fact, at low loadings between 0.25 and 1 wt % RGO, the red shift is from 488 to 547 nm. The background absorption toward the far right is due to the black carbon material at the BTO surface that at high concentrations (>1 wt %) absorbs the light but also prevents (screening) it from interacting with BTO. The observation of red shift with RGO presence is consistent with other findings on related oxide RGO systems reported elsewhere.[41,49]

The band gap was estimated from the absorbance onset, using the following equation: $E_g = hc/\lambda$, where E_g is the optical band gap, h is Planck's constant, λ is the wavelength corresponding to the onset of absorbance, and c is the velocity of light.[64−66] For the RGO-free BTO the band gap was estimated to be 2.8 eV. A shift from 2.8 to 2.54 eV (with rGBTO0.25) and to 2.26 eV (with rGBTO1) is indicative of doping effect of carbon. It is due to the Ti−O−C bond formation between Ti−OH of BTO and C from the RGO. This occurs during the thermal treatment step as indicated from the XPS analysis (discussed earlier). Similar red shift in the absorbance due to Ti−O−C bond formation has been noted in previous studies.[41,49] The absorbance measurements thus indicate that the photoactivity of the catalyst is due to the combined absorbance of UV−vis light.

6. TOWARD EFFICIENT REDUCED GRAPHENE OXIDE/MULTIMETAL OXIDE PHOTOCATALYSIS

In a recent editorial the comparison of photocatalyst performance against appropriate benchmarks was recommended.[67]

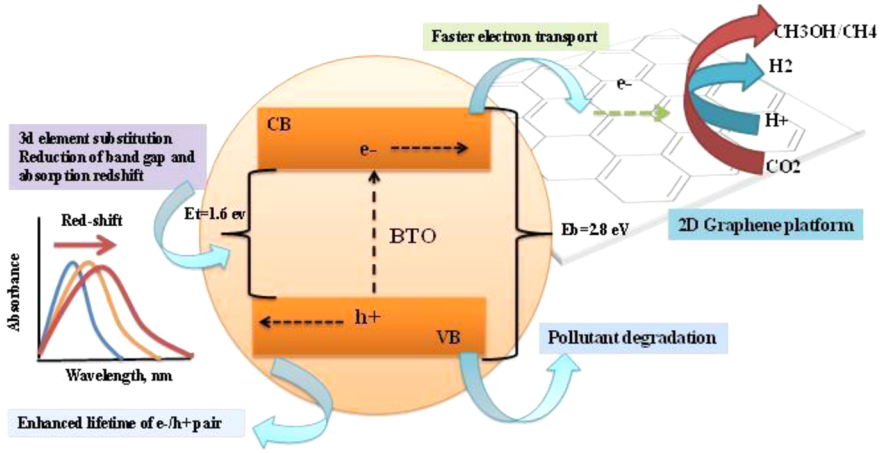

Figure 11. Depiction of the "holy grail" for nanostructures involving BTO with RGO. Though the case study reveals systematically the benefit of BTO integration to RGO for photocatalytic hydrogen evolution, the work hints at (i) the possibility of the nanostructures demonstrating multifunctionality and (ii) the extent of further improvement that can be realized should additional elements be incorporated within the pyrochlore framework.

Therefore, we carried out a systematic comparison of the BTO and rGBTO with other benchmark catalysts (shown in the Supporting Information, Figure S13). The comparison allows us to determine where the present composite catalyst stands in terms of photocatalytic hydrogen yield. Note that the catalyst produces hydrogen with the same order of magnitude as other Pt-free catalyst. Obviously, it is to be determined how Pt addition will impact H_2 yield. In rGBTO-based composites, the enhanced charge transfer from semiconductor to reduced graphene oxide (RGO) needs further investigation. In the case of multimetal oxides, such as BTO, the band gap can be engineered by various metal ion substitution, and hence the absorption onset can be tuned. Furthermore, in $A_2B_2O_7$ systems, the A and B sites can be modified independently to form $AA'BB'O_7$,[17,68] without (or with a minimal) structural distortion for enhancement in the visible light absorption. In previous studies, iron- and manganese-loaded BTO (Fe-BTO and Mn-BTO) systems[65,69] have been investigated for the improvement of visible light absorption and photocatalytic activity. The result indicated a red shift in absorption as well as an improvement in the overall hydrogen yield compared to BTO. Hence, for a proper metal ion/anion substituted BTO having a significant absorption in the visible light can be combined with reduced graphene oxide (RGO) to form a composite nanostructure with an efficient charge-separation process. Such environmentally benign, nontoxic, and green composite catalyst systems can be used for multifunctional applications (Figure 11).

7. CONCLUSIONS

A two-step electrostatic assembly method, followed by temperature-assisted reduction, has been used to synthesize a nanostructure composite consisting of reduced graphene oxide (RGO) and bismuth titanate (BTO). The composite catalyst system was characterized using various techniques such as TEM, SEM, and XPS. The TEM and SEM observations indicated a composite formation, where one or more BTO particles were wrapped with RGO. Improved photocatalytic and photoelectrochemical performance from the BTO in the presence of RGO is attributed to (i) the better interfacial contact between RGO and BTO through the self-assembly approach and (ii) the unique ability of the RGO to promote charge transport. The nanostructures exhibit a 2-fold enhancement in its photocatalytic activity. The RGO loading was optimized at 1 wt % to achieve maximum photocatalytic activity, and the composite system demonstrated excellent reusability characteristics, highlighting the stability of the nanostructure assembly. The photoluminescence and photoelectrochemical analyses indicate a better separation of charges in the composite photocatalysts. This work also demonstrates that the RGO can function as a charge separator as well as an electron sink, thus providing fundamental insights into the functioning mechanism of the nanostructure. Importantly, this also means that RGO can be a practical cost-effective substitute for expensive noble metals, thus making this process sustainable and economical. Furthermore, since the band gap of oxides such as BTO can be tuned by doping, assembly of these doped BTO or other BECONs with RGO can only be expected to additionally benefit photocatalysis and photoelectrocatalysis. The true impact of the work lies in the implementation of this approach to other related photodriven applications such as pollution control or CO_2 conversion to useful hydrocarbon products/fuels.

■ ASSOCIATED CONTENT

Supporting Information

Synthesis of bismuth titanate (BTO) and graphene oxide (GO), preparation of the photoanodes, description of the slurry reactor for the photocatalytic hydrogen generation, FTIR, Raman, and XPS analysis, time-resolved hydrogen yield of the catalyst and the composites, the comparison of the hydrogen yield obtained using the rGBTO1 with other controls. This material is available free of charge via the Internet at http://pubs.acs.org.

■ AUTHOR INFORMATION

Corresponding Author

*E-mail: ravisv@unr.edu. Fax: +1 775-327-5059. Phone: +1 775-784-4686.

Notes

The authors declare no competing financial interest.

■ ACKNOWLEDGMENTS

R.S.V. gratefully acknowledges National Science Foundation funding (NSF-CBET 1134486). The authors would like to thank S. Sarker for assistance with gathering SEM images, Prof. D. Chandra and Dr. W. M. Chien of University of Nevada, Reno for providing access to the XRD facility.

■ REFERENCES

(1) Youngblood, W. J.; Lee, S. H. A.; Maeda, K.; Mallouk, T. E. Visible Light Water Splitting Using Dye-Sensitized Oxide Semiconductors. *Acc. Chem. Res.* **2009**, *42*, 1966−1973.
(2) Higashi, M.; Domen, K.; Abe, R. Fabrication of an Efficient $BaTaO_2N$ Photoanode Harvesting a Wide Range of Visible Light for Water Splitting. *J. Am. Chem. Soc.* **2013**, *135*, 10238−10241.
(3) Osterloh, F. E. Inorganic Nanostructures for Photoelectrochemical and Photocatalytic Water Splitting. *Chem. Soc. Rev.* **2013**, *4*, 2294−2320.
(4) Maeda, K.; Domen, K. Photocatalytic Water Splitting: Recent Progress and Future Challenges. *J. Phys. Chem. Lett.* **2010**, *1*, 2655−2661.
(5) Abe, R.; Shinmei, K.; Koumura, N.; Hara, K.; Ohtani, B. Visible-Light-Induced Water Splitting Based on Two-Step Photoexcitation between Dye-Sensitized Layered Niobate and Tungsten Oxide Photocatalysts in the Presence of a Triiodide/Iodide Shuttle Redox Mediator. *J. Am. Chem. Soc.* **2013**, *135*, 16872−16884.
(6) Park, H. G.; Holt, J. K. Recent Advances in Nanoelectrode Architecture for Photochemical Hydrogen Production. *Energy Environ. Sci.* **2010**, *3*, 1028−1036.
(7) Kudo, A.; Miseki, Y. Heterogeneous Photocatalyst Materials for Water Splitting. *Chem. Soc. Rev.* **2009**, *38*, 253−278.
(8) Dhakshinamoorthy, A.; Navalon, S.; Corma, A.; Garcia, H. Photocatalytic CO_2 Reduction by TiO_2 and Related Titanium Containing Solids. *Energy Environ. Sci.* **2012**, *5*, 9217−9233.
(9) Fujishima, A.; Zhang, X.; Tryk, D. A. TiO_2 Photocatalysis and Related Surface Phenomena. *Surf. Sci. Rep.* **2008**, *63*, 515−582.
(10) Habisreutinger, S. N.; Mende, L. S.; Stolarczyk, J. K. Photocatalytic Reduction of CO_2 on TiO_2 and Other Semiconductors. *Angew. Chem., Int. Ed.* **2013**, *52*, 7372−7408.
(11) Ng, Y. H.; Ikeda, S.; Matsumura, M.; Amal, R. A Perspective on Fabricating Carbon-Based Nanomaterials by Photocatalysis and Their Applications. *Energy Environ. Sci.* **2012**, *5*, 9307−9318.
(12) Yang, J.; Voiry, D.; Joon Ahn, S.; Kang, D.; Kim, A. Y.; Chhowalla, M.; Shin, H. S. Two-Dimensional Hybrid Nanosheets of Tungsten Disulfide and Reduced Graphene Oxide as Catalysts for Enhanced Hydrogen Evolution. *Angew. Chem., Int. Ed.* **2013**, *52*, 13751−13754.
(13) Ye, M.; Chen, C.; Zhang, N.; Wen, X.; Guo, W.; Lin, C. Quantum-Dot Sensitized Solar Cells Employing Hierarchical Cu_2S Microspheres Wrapped by Reduced Graphene Oxide Nanosheets as Effective Counter Electrodes. *Adv. Energy Mater.* **2014**, *4*, DOI: 10.1002/aenm.201301564. (Accessed: 17th March 2014).
(14) Barpuzary, D.; Qureshi, M. Enhanced Photovoltaic Performance of Semiconductor-Sensitized ZnO−CdS Coupled with Graphene Oxide as a Novel Photoactive Material. *ACS Appl. Mater. Interfaces* **2013**, *5*, 11673−11682.
(15) Tu, W.; Zhou, Y.; Liu, Q.; Yan, S.; Bao, S.; Wang, X.; Xiao, M.; Zou, Z. An In Situ Simultaneous Reduction-Hydrolysis Technique for Fabrication of TiO2-Graphene 2D Sandwich-Like Hybrid Nanosheets: Graphene-Promoted Selectivity of Photocatalytic-Driven Hydrogenation and Coupling of CO_2 into Methane and Ethane. *Adv. Funct. Mater.* **2013**, *23*, 1743−1749.
(16) Iwase, A.; Ng, Y. H.; Ishiguro, Y.; Kudo, A.; Amal, R. Reduced Graphene Oxide as a Solid-State Electron Mediator in Z-Scheme Photocatalytic Water Splitting under Visible Light. *J. Am. Chem. Soc.* **2011**, *133*, 11054−11057.
(17) Murugesan, S.; Huda, M. N.; Yan, Y.; Jassim, M. M. A.; Subramanian, V. Band-Engineered Bismuth Titanate Pyrochlores for Visible Light Photocatalysis. *J. Phys. Chem. C* **2010**, *114*, 10598−10605.
(18) Modeshia, D. R.; Walton, R. I. Solvothermal Synthesis of Perovskites and Pyrochlores: Crystallisation of Functional Oxides Under Mild Conditions. *Chem. Soc. Rev.* **2010**, *39*, 4303−4325.
(19) Navalón, S.; Dhakshinamoorthy, A.; Alvaro, M.; Garcia, H. Photocatalytic CO_2 Reduction using Non-Titanium Metal Oxides and Sulfides. *ChemSusChem* **2013**, *6*, 562−577.
(20) Jing, L.; Zhou, W.; Tian, G.; Fu, H. Surface Tuning for Oxide-Based Nanomaterials as Efficient Photocatalysts. *Chem. Soc. Rev.* **2013**, *42*, 9509−9549.
(21) Qu, Y.; Duan, X. Progress, Challenge and Perspective of Heterogeneous Photocatalysts. *Chem. Soc. Rev.* **2013**, *42*, 2568−2580.
(22) Fan, W.; Lai, Q.; Zhang, Q.; Wang, Y. Nanocomposites of TiO_2 and Reduced Graphene Oxide as Efficient Photocatalysts for Hydrogen Evolution. *J. Phys. Chem. C* **2011**, *115*, 10694−10701.
(23) Meng, F.; Li, J.; Cushing, S. K.; Zhi, M.; Wu, N. Solar Hydrogen Generation by Nanoscale p−n Junction of p-type Molybdenum Disulfide/n-type Nitrogen-Doped Reduced Graphene Oxide. *J. Am. Chem. Soc.* **2013**, *135*, 10286−10289.
(24) Som, T.; Troppenz, G. V.; Wendt, R. R.; Wollgarten, M.; Rappich, J.; Emmerling, F.; Rademann, K. Graphene Oxide/α-Bi_2O_3 Composites for Visible-Light Photocatalysis, Chemical Catalysis, and Solar Energy Conversion. *ChemSusChem* **2014**, *7*, 854−865.
(25) Hernández-Alonso, M. D.; Fresno, F.; Suáreza, S.; Coronado, J. M. Development of Alternative Photocatalysts to TiO_2: Challenges and Opportunities. *Energy Environ. Sci.* **2009**, *2*, 1231−1257.
(26) Murugesan, S.; Subramanian, V. Robust Synthesis of Bismuth Titanate Pyrochlore Nanorods and Their Photocatalytic Applications. *Chem. Commun.* **2009**, 5109−5111.
(27) Hummers, W. S.; Offeman, R. E. Preparation of Graphitic Oxide. *J. Am. Chem. Soc.* **1958**, *80*, 1339−1339.
(28) Chen, Z.; Liu, S.; Yang, M. Q.; Xu, Y. J. Synthesis of Uniform CdS Nanospheres/Graphene Hybrid Nanocomposites and Their Application as Visible Light Photocatalyst for Selective Reduction of Nitro Organics in Water. *ACS Appl. Mater. Interfaces* **2013**, *5*, 4309−4319.
(29) Liu, S.; Chen, Z.; Zhang, N.; Tang, Z. R.; Xu, Y. J. An Efficient Self-Assembly of CdS Nanowires−Reduced Graphene Oxide Nanocomposites for Selective Reduction of Nitro Organics under Visible Light Irradiation. *J. Phys. Chem. C* **2013**, *117*, 8251−8261.
(30) Yang, M. Q.; Weng, B.; Xu, Y. J. Improving the Visible Light Photoactivity of In_2S_3−Graphene Nanocomposite via a Simple Surface Charge Modification Approach. *Langmuir* **2013**, *29*, 10549−10558.
(31) Zhang, N.; Zhang, Y.; Pan, X.; Yang, M. Q.; Xu, Y. J. Constructing Ternary CdS−Graphene−TiO_2 Hybrids on the Flatland of Graphene Oxide with Enhanced Visible-Light Photoactivity for Selective Transformation. *J. Phys. Chem. C* **2012**, *116*, 18023−18031.
(32) Liu, S.; Yang, M. Q.; Xu, Y. J. Surface Charge Promotes the Synthesis of Large, Flat Structured Graphene−(CdS Nanowire)−TiO_2 Nanocomposites as Versatile Visible Light Photocatalysts. *J. Mater. Chem. A* **2014**, *2*, 430−440.
(33) Zhang, N.; Zhang, Y.; Xu, Y. J. Recent Progress on Graphene-Based Photocatalysts: Current Status and Future Perspectives. *Nanoscale* **2012**, *4*, 5792−5813.
(34) Yang, M. Q.; Xu, Y. J. Selective Photoredox Using Graphene-Based Composite Photocatalysts. *Phys. Chem. Chem. Phys.* **2013**, *15*, 19102−19118.
(35) Zhang, N.; Yang, M. Q.; Tang, Z. R.; Xu, Y. J. Toward Improving the Graphene Semiconductor Composite Photoactivity via the Addition of Metal Ions as Generic Interfacial Mediator. *ACS Nano* **2014**, *8*, 623−633.
(36) Zhang, Y.; Tang, Z. R.; Fu, X.; Xu, Y. J. Engineering the Unique 2D Mat of Graphene to Achieve Graphene-TiO_2 Nanocomposite for Photocatalytic Selective Transformation: What Advantage does Graphene Have over Its Forebear Carbon Nanotube? *ACS Nano* **2011**, *5*, 7426−7435.
(37) Zhang, Y.; Tang, Z. R.; Fu, X.; Xu, Y. J. TiO_2-Graphene Nanocomposites for Gas-Phase Photocatalytic Degradation of Volatile

Aromatic Pollutant: Is TiO_2-Graphene Truly Different from Other TiO_2-Carbon Composite Materials? *ACS Nano* **2010**, *4*, 7303−7314.
(38) Li, X.; Wang, H.; Robinson, J. T.; Sanchez, H.; Diankov, G.; Dai, H. Simultaneous Nitrogen Doping and Reduction of Graphene Oxide. *J. Am. Chem. Soc.* **2009**, *131*, 15939−15944.
(39) Choi, E. Y.; Han, T. H.; Hong, J.; Kim, J. E.; Lee, S. H.; Kim, H. W.; Kim, S. O. Noncovalent Functionalization of Graphene with End-Functional Polymers. *J. Mater. Chem.* **2010**, *20*, 1907−1912.
(40) Xu, Y.; Bai, H.; Lu, G. W.; Li, C.; Shi, G. Flexible Graphene Films via the Filtration of Water-Soluble Noncovalent Functionalized Graphene Sheets. *J. Am. Chem. Soc.* **2008**, *130*, 5856−5857.
(41) Cheng, G.; Akhtar, M. S.; Yang, O. B.; Stadler, F. J. Novel Preparation of Anatase TiO_2@Reduced Graphene Oxide Hybrids for High-Performance Dye-Sensitized Solar Cells. *ACS Appl. Mater. Interfaces* **2013**, *5*, 6635−6642.
(42) Gupta, S.; Ramamaurthy, P. C.; Madras, G. Synthesis and Characterization of Flexible Epoxy Nanocomposites Reinforced with Amine Functionalized Alumina Nanoparticles: A Potential Encapsulant For Organic Devices. *Polym. Chem.* **2011**, *2*, 221−228.
(43) Wang, J.; Liang, S.; Ma, L.; Ding, S.; Yu, X.; Zhou, L.; Wang, Q. One-Pot Synthesis of Cds−Reduced Graphene Oxide 3D Composites with Enhanced Photocatalytic Properties. *CrystEngComm* **2014**, *16*, 399−405.
(44) Zhao, F.; Li, H.; Jiang, Y.; Wang, X.; Mu, X. Co-Immobilization of Multi-Enzyme on Control-Reduced Graphene Oxide by Non-Covalent Bonds: An Artificial Biocatalytic System for the One-Pot Production of Gluconic Acid from Starch. *Green Chem.* **2014**, *16*, 2558−2565.
(45) Gong, F.; Xu, X.; Zhou, G.; Wang, Z. S. Enhanced Charge Transportation in a Polypyrrole Counter Electrode via Incorporation of Reduced Graphene Oxide Sheets for Dye-Sensitized Solar Cells. *Phys. Chem. Chem. Phys.* **2013**, *15*, 546−552.
(46) Lee, J. S.; You, K. H.; Park, C. B. Highly Photoactive, Low Bandgap TiO_2 Nanoparticles Wrapped by Graphene. *Adv. Mater.* **2012**, *24*, 1084−1088.
(47) Stankovich, S.; Dikin, D. A.; Piner, R. D.; Kohlhaas, K. A.; Kleinhammes, A.; Jia, Y.; Wu, Y.; Nguyen, S. T.; Ruoff, R. S. Synthesis of Graphene-Based Nanosheets via Chemical Reduction of Exfoliated Graphite Oxide. *Carbon* **2007**, *45*, 1558−1565.
(48) Guo, H. L.; Su, P.; Kanga, X.; Ning, S. K. Synthesis and Characterization of Nitrogen-Doped Graphene Hydrogels by Hydrothermal Route with Urea as Reducing-Doping Agents. *J. Mater. Chem. A* **2013**, *1*, 2248−2255.
(49) Xiang, Q.; Yu, J.; Jaroniec, M. Enhanced Photocatalytic H_2-Production Activity of Graphene-Modified Titania Nanosheets. *Nanoscale* **2011**, *3*, 3670−3678.
(50) Ganguly, A.; Sharma, S.; Papakonstantinou, P.; Hamilton, J. Probing the Thermal Deoxygenation of Graphene Oxide using High Resolution In Situ X-Ray based Spectroscopies. *J. Phys. Chem. C* **2011**, *115*, 17009−17019.
(51) Zhang, H.; Lv, X.; Li, Y.; Wang, Y.; Li, J. P25-Graphene Composite as a High Performance Photocatalyst. *ACS Nano* **2010**, *4*, 380−386.
(52) Mukherji, A.; Seger, B.; Lu, G. Q.; Wang, L. Nitrogen Doped $Sr_2Ta_2O_7$ Coupled with Graphene Sheets as Photocatalysts for Increased Photocatalytic Hydrogen Production. *ACS Nano* **2011**, *5*, 3483−3492.
(53) Yang, S.; Feng, X.; Ivanovici, S.; Mullen, K. Fabrication of Graphene-Encapsulated Oxide Nanoparticles: Towards High-Performance Anode Materials for Lithium Storage. *Angew. Chem., Int. Ed.* **2010**, *49*, 8408−8411.
(54) Jia, L.; Wang, D. H.; Huang, Y. X.; Xu, A. W.; Yu, H. Q. Highly Durable N-Doped Graphene/CdS Nanocomposites with Enhanced Photocatalytic Hydrogen Evolution from Water under Visible Light Irradiation. *J. Phys. Chem. C* **2011**, *115*, 11466−11473.
(55) Li, Q.; Guo, B.; Yu, J.; Ran, J.; Zhang, B.; Yan, H.; Gong, J. R. Highly Efficient Visible-Light-Driven Photocatalytic Hydrogen Production of CdS-Cluster-Decorated Graphene Nanosheets. *J. Am. Chem. Soc.* **2011**, *133*, 10878−10884.
(56) Lv, X. J.; Fu, W. F.; Chang, H. X.; Zhang, H.; Cheng, J. S.; Zhang, G. J.; Song, Y.; Hu, C. Y.; Li, J. H. Hydrogen Evolution from Water Using Semiconductor Nanoparticle/Graphene composite Photocatalysts Without Noble Metals. *J. Mater. Chem.* **2012**, *22*, 1539−1546.
(57) Choi, H. J.; Kang, M. Hydrogen Production from Methanol/Water Decomposition in a Liquid Photosystem Using the Anatase Structure of Cu Loaded TiO_2. *Int. J. Hydrogen Energy* **2007**, *32*, 3841−3848.
(58) Arana, J.; Diaz, O. G.; Saracho, M. M.; Rodriguez, J. M. D.; Melian, J. A. H.; Pena, J. P. Photocatalytic Degradation of Formic Acid Using Fe/TiO_2 Catalysts: The Role of Fe^{3+}/Fe^{2+} Ions in the Degradation Mechanism. *Appl. Catal., B* **2001**, *32*, 49−61.
(59) Kandiel, T. A.; Ivanova, I.; Bahnemann, D. W. Long-Term Investigation of the Photocatalytic Hydrogen Production on Platinized TiO_2: An Isotopic Study. *Energy Environ. Sci.* **2014**, *7*, 1420−1425.
(60) Bard, A. J.; Faulkner, L. R. Chapter 10. In *Electrochemical Methods Fundamentals and Applications,* 2nd ed.; John Wiley & Sons: New York, 2001; pp 368−416.
(61) Wang, Y.; Wang, F.; He, J. Controlled Fabrication and Photocatalytic Properties of A Three-Dimensional ZnO Nanowire/Reduced Graphene Oxide/Cds Nanostructures on Carbon Cloth. *Nanoscale* **2013**, *5*, 11291−11297.
(62) Chen, Y.; Ge, H.; Wei, L.; Li, Z.; Yuan, R.; Liu, P.; Fu, X. Reduction Degree of Reduced Graphene Oxide (RGO) Dependence of Photocatalytic Hydrogen Evolution Performance over RGO/$ZnIn_2S_4$ Nanocomposites. *Catal. Sci. Technol.* **2013**, *3*, 1712−1717.
(63) Pradhan, G. K.; Padhi, D. K.; Parida, K. M. Fabrication of α-Fe_2O_3 Nanorod/RGO Composite: A Novel Hybrid Photocatalyst for Phenol Degradation. *ACS Appl. Mater. Interfaces* **2013**, *5*, 9101−9110.
(64) Shimizu, K.; Tsuji, Y.; Hatamachi, T.; Toda, K.; Kodama, T.; Sato, M.; Kitayama, Y. Photocatalytic water splitting on hydrated layered Perovskite tantalate $A_2SrTa_2O_7{\cdot}nH_2O$ (A = H, K, and Rb). *Phys. Chem. Chem. Phys.* **2004**, *6*, 1064−1069.
(65) Allured, B.; DelaCruz, S.; Darling, T.; Huda, M. N.; Subramanian, V. Enhancing the Visible Light Absorbance Of $Bi_2Ti_2O_7$ Through Fe-Substitution and its Effects on Photocatalytic Hydrogen Evolution. *Appl. Catal., B* **2014**, *144*, 261−268.
(66) Puangpetcha, T.; Sreethawonga, T.; Yoshikawa, S.; Chavadej, S. Hydrogen Production from Photocatalytic Water Splitting over Mesoporous-Assembled $SrTiO_3$ Nanocrystal-Based Photocatalysts. *J. Mol. Catal. A: Chem.* **2009**, *312*, 97−106.
(67) Buriak, J. M. Your Research Results Look Compelling, but Are They Reliable? *Chem. Mater.* **2014**, *26*, 2211−2213.
(68) Kudo, A.; Kato, H.; Nakagawa, S. Water Splitting into H_2 and O_2 on New $Sr_2M_2O_7$ (M = Nb and Ta) Photocatalysts with Layered Perovskite Structures: Factors Affecting the Photocatalytic Activity. *J. Phys. Chem. B* **2000**, *104*, 571−575.
(69) Gupta, S.; Leon, L. D.; Subramanian, V. Mn-Modified $Bi_2Ti_2O_7$ Photocatalysts: Bandgap Engineered Multifunctional Photocatalysts for Hydrogen Generation. *Phys. Chem. Chem. Phys.* **2014**, *16*, 12719−12727.